(Received 6 May 2026, Accepted 29 June 2026, Scheduled 9 July 2026)

A Miniaturized Circularly Polarized Antenna with Embedded Metasurface Patches

Xu Tan[1], Han Lin[1,*], Zhonggen Wang[1], and Wenyan Nie[2]

[1] School of Electrical and Information Engineering, Anhui University of Science and Technology, Huainan 232001, China
[2] School of Mechanical and Electrical Engineering, Huainan Normal University, Huainan 232001, China

ABSTRACT: This study proposes a high-performance miniaturized wideband circularly polarized (CP) metasurface (MTS) antenna for WLAN and 5 GHz wireless communication systems. The design innovatively utilizes a hybrid embedded structure, where regular octagonal patches are incorporated into the gaps of modified X-shaped primary radiating elements to increase edge capacitance and lower resonant frequency, thereby achieving antenna miniaturization. To effectively excite the orthogonal degenerate modes required for CP radiation, a characteristic mode analysis (CMA) was employed to guide the design of the feed network. A feeding structure consisting of a hook-shaped microstrip line and a symmetrical stepped cross-slot is designed to achieve CP excitation via a 90° phase delay introduced by path length differences. Measured results demonstrate that the antenna achieves a −10 dB impedance bandwidth of 34.2% (4.38–6.19 GHz) and a 3 dB axial ratio (AR) bandwidth of 23.9% (4.68–5.95 GHz). Regarding radiation characteristics, the radiation efficiency remained stable above 75%, and the peak realized gain reached 5.26 dBic. The experimental results verified that the proposed design achieved stable CP and radiation performance within a miniaturized footprint.

1. INTRODUCTION

Wireless communication technology is developing rapidly, and CP antennas can effectively overcome the limitations of traditional linearly polarized antennas in complex communication scenarios owing to their unique electromagnetic radiation characteristics [1–3]. Therefore, CP antennas exhibit significant advantages in satellite communications, navigation, and positioning, and WLAN/5 GHz wireless communications [4–6]. However, conventional planar CP antennas, such as microstrip patches, are limited by their high Q-factor resonant characteristics, making it difficult to simultaneously achieve broadband performance, high gain, and miniaturized size. Although conventional techniques, such as stacking patches or employing thick substrates, can extend the bandwidth to some extent, they inevitably lead to increased surface-wave losses and reduced radiation efficiency.

To overcome the inherent bottlenecks of traditional planar CP antennas, metasurface technology has recently been widely introduced into antenna design [7]. Its subwavelength unit cell structure enables wavefront modulation and resonant mode expansion within a low-profile configuration [8]. To further meet the requirements of miniaturized systems, various methods have been proposed to miniaturize MTS antennas. In [9], a miniaturized antenna was designed based on the analysis of the dispersion characteristics of an MTS structure; however, traditional rectangular MTS units exhibit limited potential for further miniaturization. In [10], miniaturization was attempted by loading parasitic loops around a cross-dipole structure; however, this multi-layer configuration inevitably led to an increased profile height and assembly difficulties. Furthermore, although loading quasi-fractal slots, as mentioned in [11], can effectively extend the current path to a lower resonant frequency, such designs often result in linearly polarized radiation and are unsuitable for CP scenarios. To achieve CP miniaturization, a structure utilizing microstrip line loading on patches was proposed in [12]; however, its achievable 3-dB axial ratio bandwidth (ARBW) was restricted to only 8.5%. Consequently, structural complexity, excessive profile heights, and narrow CP bandwidths remain the primary drawbacks of these existing studies. In contrast, multi-mode excitation designs with simplified feeding structures have maintained significant research interest owing to their potential for bandwidth extension [13].

Generally, employing a simplified slot-coupling structure is a highly cost-effective approach for exciting CP antennas compared with complex feed networks. Therefore, systematically increasing the ARBW of slot-coupled miniaturized MTS antennas is a valuable research objective. To address this, CMA has been introduced to predict current modal behaviors and reveal underlying operating mechanisms without the need for external excitation sources [14]. This method provides clear guidance for miniaturization and wideband CP design, while avoiding inefficiencies of blind parameter optimization [15].

In this paper, a miniaturized wideband CP MTS antenna is proposed for WLAN and 5 GHz communications. Distinct from conventional multi-layer or asymmetric designs, a planar hybrid structure is developed by nesting regular octagonal patches within the gaps of modified X-shaped elements. The multi-angled edges of the regular octagonal patches effectively enlarge the capacitive coupling perimeter and elongate the sur-

* Corresponding author: Han Lin (hanlin@aust.edu.cn).

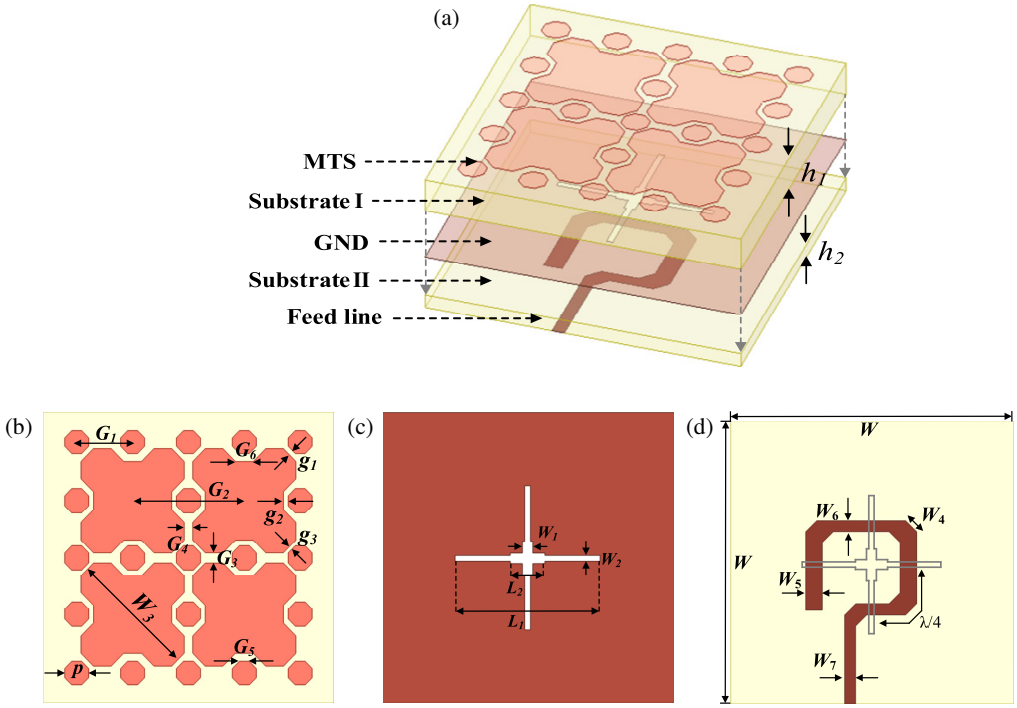

FIGURE 1. Configuration of the proposed antenna. (a) 3-D view, (b) top view, (c) top view of the ground plane, (d) bottom view.

face current paths. This unique geometry lowers the resonant frequency via increased edge capacitance, while expanding the effective current distribution for orthogonal degenerate modes without sacrificing structural symmetry. Guided by CMA, a hook-shaped microstrip line and a symmetrical stepped cross-slot are utilized to introduce the required 90° phase delay. Simulation and measurement results verify the excellent performance of the proposed antenna in terms of operating bandwidth, CP purity, and radiation efficiency, which can meet the practical application requirements of modern miniaturized wireless terminals in WLAN and 5 GHz communication scenarios.

2. ANTENNA DESIGN PROCESS

2.1. Antenna Geometry

The geometry of the proposed antenna is illustrated in Fig. 1. From top to bottom, the antenna consists of an MTS layer, an upper dielectric substrate as Substrate I, a GND layer, a lower dielectric substrate as Substrate II, and a bottom feedline layer. Substrate I has a thickness h_1 of 2.65 mm, and Substrate II has a thickness h_2 of 1.1 mm. Both substrates are made of FR-4 material with a relative permittivity of $\varepsilon_r = 4.4$ and a loss tangent of $\tan\delta = 0.025$. These two layers serve distinct physical functions in the design. Substrate I provides the necessary dielectric spacing for the MTS, where its thickness primarily affects the resonant frequency and operating bandwidth. Substrate II supports the bottom feed network, with its dielectric properties and thickness governing the characteristic impedance of the microstrip line and electromagnetic coupling through the stepped cross-slot.

The MTS layer is composed of 2×2 hybrid radiating elements, where each primary radiating patch adopts an improved X-shaped structure. Regular octagonal patches are embedded in the gaps of these primary patches to increase edge capacitance and lower resonant frequency, thereby achieving antenna miniaturization. The GND layer, situated at the bottom of the upper substrate, features an etched symmetrical stepped cross-slot. The bottom feedline layer employs a hook-shaped microstrip line in a series-fed configuration. The electromagnetic energy from the bottom microstrip line is coupled to the top MTS layer through the symmetrical stepped cross-slot on the GND layer. The optimized structural parameters are listed in Table 1. To further elucidate the miniaturization mechanism of the proposed antenna, a theoretical equivalent circuit analysis is discussed in the following section.

2.2. Miniaturization of the MTS

As described in [16], the surface impedance of a conventional MTS can be modeled as the equivalent circuit shown in Fig. 2(a). This circuit consists of an inductance L_d from the ground plane and a capacitance C_0 introduced by the gap between two adjacent MTS units. The resonant frequency condition can be expressed as

$$f_0 = \frac{1}{2\pi\sqrt{(L_g + L_d)\,C_0}} \tag{1}$$

Consequently, the resonant frequency can be reduced by introducing additional capacitance and inductance. The equivalent inductance L_d is typically influenced by the substrate thickness h_1, whereas the equivalent capacitance C_0 is governed by both the width of MTS elements and the inter-element gap. Therefore, in this study, additional capacitance is introduced through the MTS structure, as shown in Fig. 2(b).

TABLE 1. Antenna parameter dimensions.

Parameter	W	W_1	W_2	L_1	L_2	G_1	G_2	G_3	G_4
Size (mm)	25.5	0.7	0.5	12.6	2.5	4.89	9.79	0.89	0.74
Parameter	G_5	G_6	h_1	h_2	W_3	p	g_1	g_2	g_3
Size (mm)	0.87	1.55	2.65	1.1	11.24	2.11	0.43	0.42	0.30
Parameter	d	a	b	c	W_4	W_5	W_6	W_7	
Size (mm)	28.2	7.11	4.89	6.97	1.41	1.5	1.0	1.0	

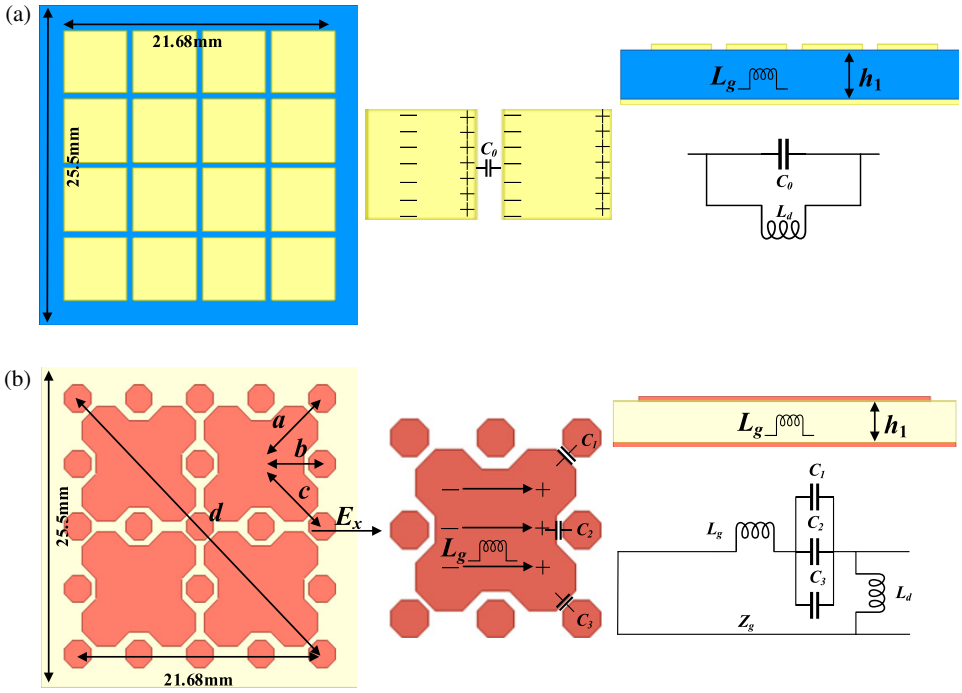

FIGURE 2. (a) Conventional MTS and (b) hybrid embedded MTS.

When the hybrid MTS structure is exposed to an incident electric field E_x in the x-direction, the electrons on the MTS are stimulated and move along the x-axis, thereby producing a surface current J. The moving electrons form capacitance at the adjacent gaps; thus, edge capacitances C_1, C_2, and C_3 are introduced. Additionally, the MTS unit itself contributes to the strip inductance L_g, whereas the ground plane provides inductance L_d. Therefore, the equivalent circuit model for the hybrid MTS, shown in Fig. 2(b), is composed of inductances L_g and L_d and capacitances C_1, C_2, and C_3 in parallel. The resonant frequency f_0 can be expressed as

$$f_0 = \frac{1}{2\pi\sqrt{(L_g + L_d)(C_1 + C_2 + C_3)}} = \frac{1}{2\pi\sqrt{(L_g + L_d)C_{total}}} \quad (2)$$

The C_i, L_d, and L_g in the formula can be approximated as follows:

$$C_1 = \frac{w_3\varepsilon_0(1+\varepsilon_r)}{\pi}\cosh^{-1}\left(\frac{a}{g_1}\right) = \frac{w_3\varepsilon_0(1+\varepsilon_r)}{\pi}\cosh^{-1}\left(\frac{d}{4g_1}\right) \quad (3)$$

$$C_2 = \frac{w_3\varepsilon_0(1+\varepsilon_r)}{\pi}\cosh^{-1}\left(\frac{b}{g_2}\right) = \frac{w_3\varepsilon_0(1+\varepsilon_r)}{\pi}\cosh^{-1}\left(\frac{d\sqrt{2}}{8g_2}\right) \quad (4)$$

$$C_3 = \frac{w_3\varepsilon_0(1+\varepsilon_r)}{\pi}\cosh^{-1}\left(\frac{c}{g_3}\right) = \frac{w_3\varepsilon_0(1+\varepsilon_r)}{\pi}\cosh^{-1}\left(\frac{d}{4g_3}\right) \quad (5)$$

$$L_g = \frac{2Z_0}{\omega}\tan\left(\frac{\omega\sqrt{\mu_0\varepsilon_0}\sqrt{\frac{(\varepsilon_r+1)}{2}}(w_3-2p)}{2}\right) \quad (6)$$

$$L_d = \mu h_1 \quad (7)$$

where ε_0 and μ_0 represent the permittivity and permeability of the free space, respectively; ε_r and μ denote the relative permittivity and permeability of the dielectric substrate, respectively;

h_1 is the substrate thickness; ω is the angular frequency; Z_0 is the characteristic impedance of free space.

To clarify, this equivalent-circuit model is established based on the quasi-static approximation, and the fringing fields within the narrow gaps are evaluated using the conformal mapping method. The variables a, b, c, and d correspond to the specific geometric distances between the modified X-shaped patches and regular octagonal patches, as depicted in Fig. 2(b), whereas p denotes the width of the small octagonal patch. Since the unit dimension is much smaller than the operating wavelength, these formulas are dimensionally consistent and physically valid for the targeted 5 GHz band.

From a physical perspective, the specific arrangement of the embedded regular octagonal patches and the modified X-shaped elements directly determines the resonance characteristics of the MTS. The narrow gaps between these metal geometries introduce additional capacitive coupling, thereby significantly increasing the equivalent edge capacitances (C_1, C_2, C_3). According to the equivalent circuit model, this enhanced total capacitance naturally shifts the resonant frequency downward. Consequently, antenna miniaturization is successfully achieved without enlarging the physical footprint.

2.3. Characteristic Mode Analysis

To effectively excite the proposed MTS structure and design an appropriate feed network, the CMA method is adopted in this section to guide antenna analysis. According to the CMA theory, the total current distributed on the surface of a perfect electric conductor (PEC) can be described as a linear superposition of the characteristic currents as follows:

$$J = \sum_n \alpha_n J_n \tag{8}$$

where α_n is the modal weighting coefficient, employed to characterize the proportion of the n-th characteristic current J_n to the total current J. When external excitation is considered, α_n is expressed as

$$\alpha_n = \frac{\langle J_n, E^i \rangle}{1 + j\lambda_n} \tag{9}$$

where λ_n is the eigenvalue corresponding to the characteristic current J_n, and E^i denotes the incident electric field. The denominator of α_n is defined as the modal significance (MS) and can be expressed as

$$\mathrm{MS} = \frac{1}{|1 + j\lambda_n|} \tag{10}$$

MS represents the inherent property of each mode and is solely dependent on the antenna structure, with a value range of [0, 1]. An MS value approaching 1 indicates that the mode is more prone to resonance, leading to more effective antenna radiation. Therefore, the desired antenna characteristics can be obtained by strongly exciting the target modes at the desired resonant frequency, avoiding the excitation of undesired modes, and determining a suitable feed structure.

To investigate the operating mechanism, the commercial software Computer Simulation Technology (CST) was used to perform CMA on the conventional MTS and the proposed hybrid embedded MTS geometries without feeding structures. In these simulations, the ground plane and MTS radiation layers were modeled as perfect electric conductors, with both the substrate and ground plane infinitely extended.

Based on the characteristic mode simulation, Fig. 3 presents the MS curves of the first four modes for both the conventional rectangular patch MTS (denoted as $J_{O1} \sim J_{O4}$) and the proposed hybrid embedded MTS (denoted as $J_1 \sim J_4$). For the conventional structure, J_{O1} and J_{O2} constitute a pair of degenerate modes that resonate (MS = 1) at approximately 7.8 GHz, while the remaining two modes are ideal for omnidirectional radiation. Upon adopting the hybrid structure, the resonant frequencies of the dominant degenerate modes J_1 and J_2 shifted to approximately 6.1 GHz, and all four modes of the proposed structure shifted toward the lower frequency band. In other words, for an MTS with the same physical dimensions, the proposed hybrid structure exhibits a lower resonant frequency (from 7.8 GHz to 6.1 GHz). Because the physical area of an antenna is roughly proportional to the square of its resonant wavelength, this frequency shift translates to an equivalent physical footprint reduction of approximately 38.8% compared to a conventional rectangular MTS operating at the same frequency. This observation is consistent with the equivalent circuit analysis.

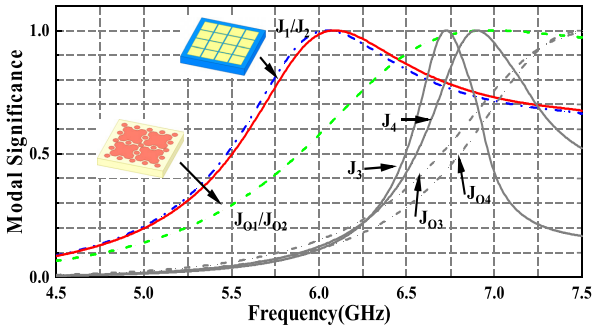

FIGURE 3. Simulated modal significance (MS) of the conventional and proposed MTSs.

To further reveal the physical characteristics of these modes, Figs. 4 and 5 illustrate the boundary setups, far-field radiation characteristics, and modal currents of the conventional and hybrid structures at their respective resonant frequencies. It can be observed that the surface current distributions of J_1 and J_2 are mutually orthogonal, and the most intense currents for all modes are concentrated on the four modified patches in the central region. To acquire the desired CP radiation characteristics, these two orthogonal modes (J_1 and J_2) should be selected and synchronously excited with a 90° phase difference.

With the desired modes identified, CMA was subsequently applied to the complete fed structure to evaluate its practical excitation capability, explicitly including the ground slot and feedline. As shown in Fig. 6, the extracted modal weighting coefficients (MWCs) clearly indicate that the desired orthogonal modes (J_1 and J_2) are effectively excited with equal amplitudes around the center frequency. Meanwhile, the undesired

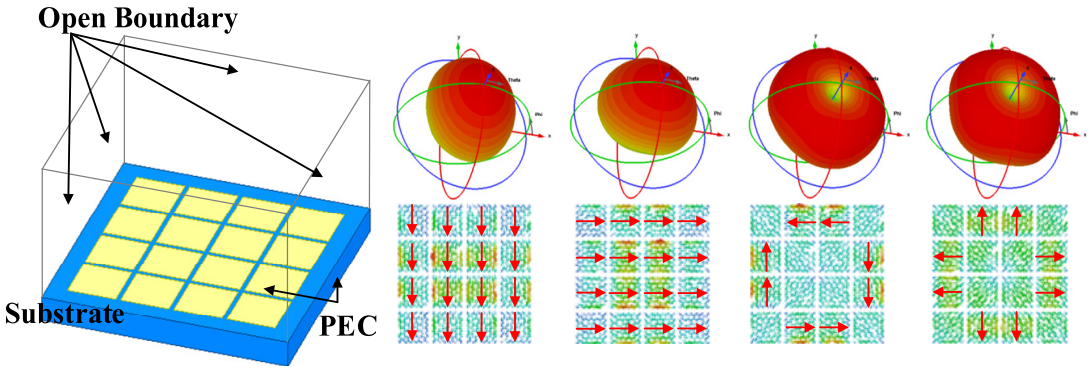

FIGURE 4. CMA of the conventional MTS: boundary setup, radiation patterns, and modal currents of $J_{O1} \sim J_{O4}$ at 7.8 GHz.

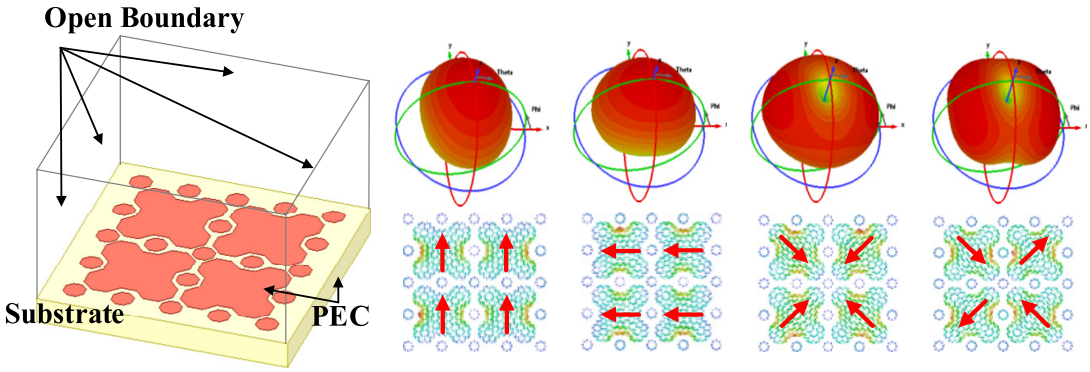

FIGURE 5. CMA of the proposed MTS: boundary setup, radiation patterns, and modal currents of $J_1 \sim J_4$ at 6.1 GHz.

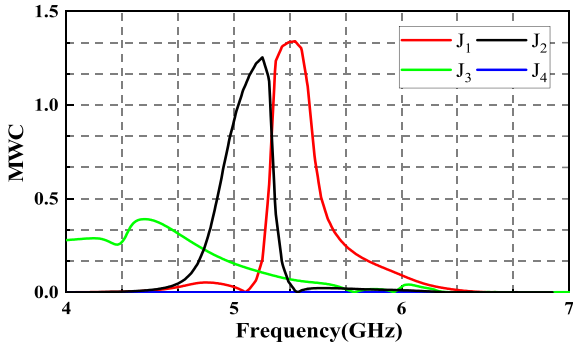

FIGURE 6. Modal weighting coefficients (MWCs) of the complete fed antenna.

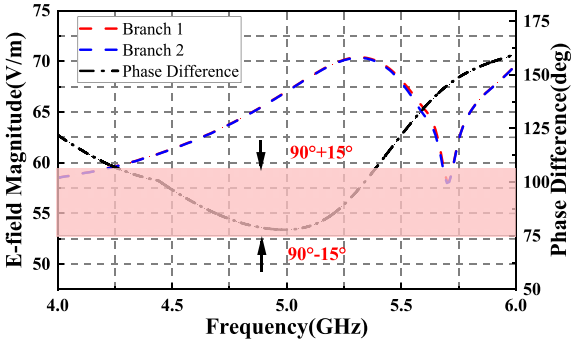

FIGURE 7. Simulated E-field magnitudes and relative phase difference of the two orthogonal slot branches.

higher-order modes (J_3 and J_4) are significantly suppressed to near-zero levels. This confirms that the proposed sequential coupling feed network successfully isolates and excites the target radiation modes.

Based on the analyzed current distribution characteristics, a symmetrical stepped cross-slot and a hook-shaped microstrip line were combined as the feed. In this series-fed structure, the microstrip line sequentially crosses the two orthogonal branches of the cross-slot. To introduce the required 90° phase difference, the path length between these two coupling points is set to approximately a quarter of the guided wavelength ($\lambda_g/4$) at 5.315 GHz. To verify this mechanism, simulated E-field probes were utilized to extract the local electric fields. As shown in Fig. 7, the E-field magnitudes of the two orthogonal slot branches (denoted as Branch 1 and Branch 2) are highly consistent across the operating band, indicating a well-balanced power division. Furthermore, as the frequency increases from 4.0 to 6.0 GHz, the phase difference first decreases and then increases. Within the 3-dB axial ratio (AR) bandwidth (4.73–5.91 GHz), the phase difference is maintained within $90° \pm 15°$, crossing 90° near 5.315 GHz. This quantitatively confirms the synchronous excitation of modes J_1 and J_2 with a 90° phase difference, generating right-hand CP (RHCP) radiation along the $+z$-direction.

2.4. Antenna Parameters Analysis

Key structural parameters were investigated to optimize the antenna performance, as shown in Fig. 8. Decreasing the gaps g_2 and g_3 effectively increases the inter-element coupling capaci-

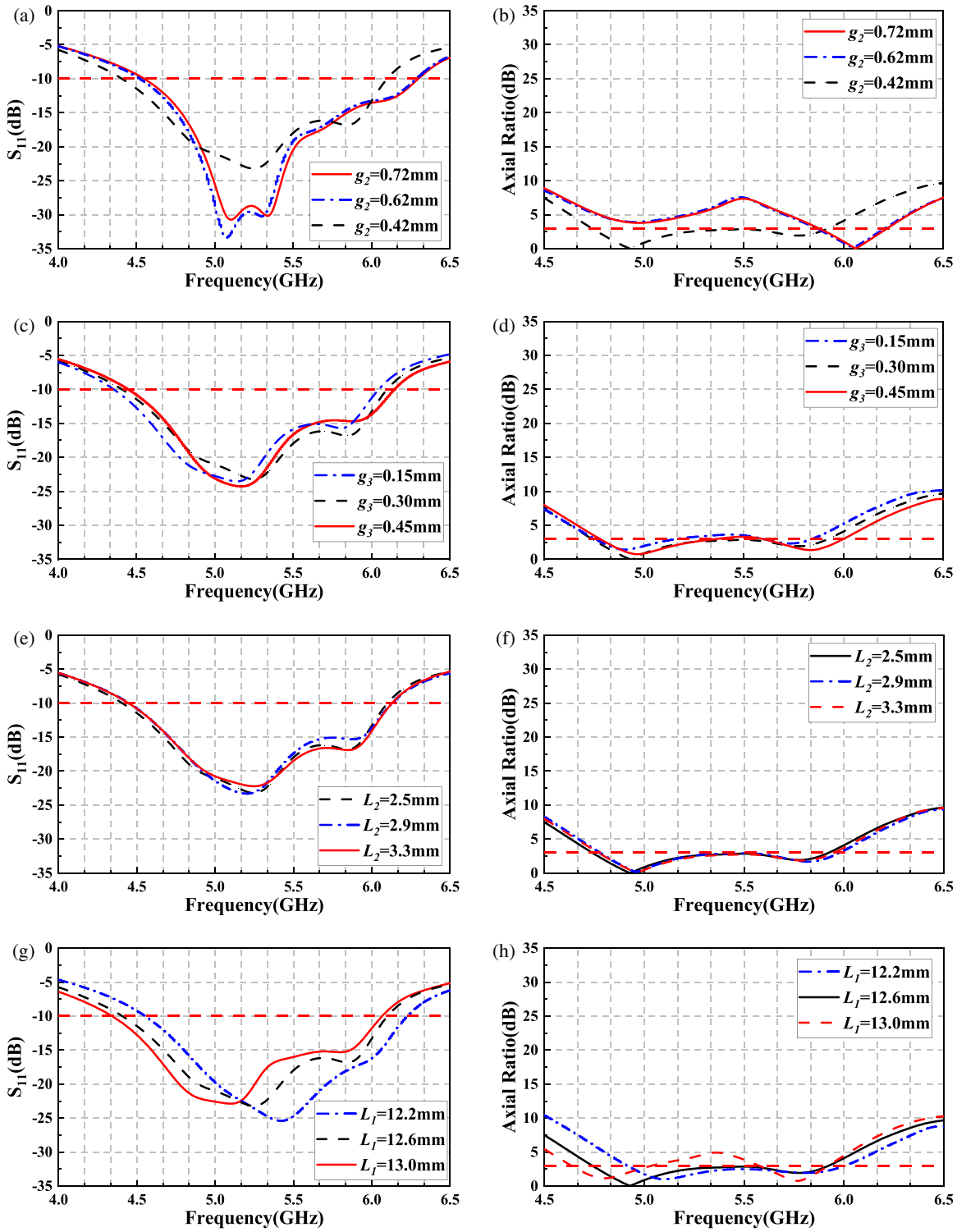

FIGURE 8. S parameters and axial ratio for antenna parameter analysis: (a) S_{11} of g_2, (b) AR of g_2, (c) S_{11} of g_3, (d) AR of g_3, (e) S_{11} of L_2, (f) AR of L_2, (g) S_{11} of L_1, and (h) AR of L_1.

tance between the main and octagonal patches, shifting both the impedance resonances and axial ratio minimums toward lower frequencies to significantly facilitate antenna miniaturization. Simultaneously, adjusting the slot dimensions L_1 and L_2 controls the electromagnetic coupling strength, which improves the equivalent input impedance and ensures the balanced, equal-amplitude excitation of orthogonal degenerate modes for high CP purity. Consequently, the optimized parameters were determined as $g_2 = 0.42$ mm, $g_3 = 0.30$ mm, $L_1 = 12.6$ mm, and $L_2 = 2.5$ mm.

To visually verify the CP performance of the optimized antenna, Fig. 9 presents the instantaneous surface currents and underlying electric-field distributions at 4.93 GHz across different excitation phases (0°, 90°, 180°, and 270°). As depicted, with

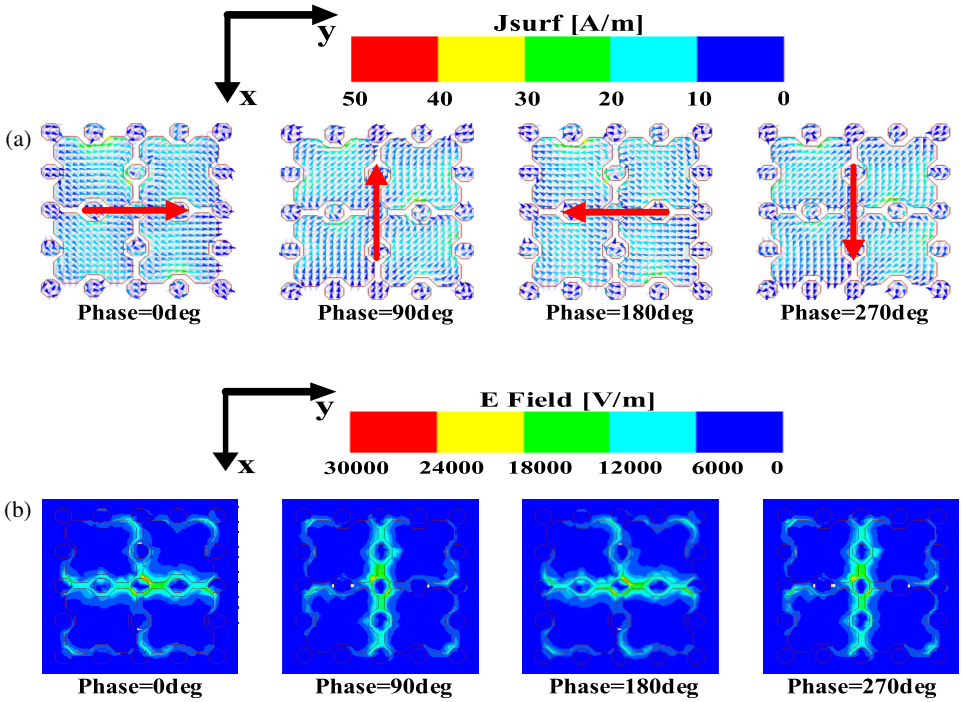

FIGURE 9. Instantaneous field distributions of the proposed antenna at 4.93 GHz across different excitation phases: (a) surface current distributions and (b) underlying electric field distributions.

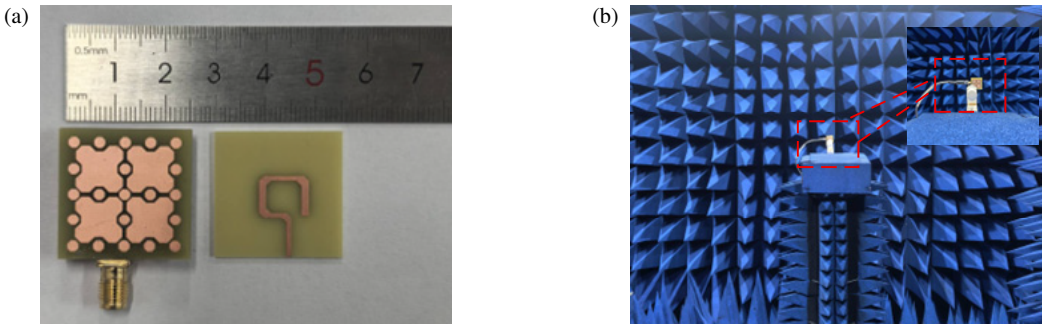

FIGURE 10. Photograph of the prototype in the measurement.

an increase in the excitation phase, the resultant current vector on the antenna surface (indicated by the red arrows) exhibits a distinct counterclockwise rotation. Simultaneously, the concentrated regions of the underlying electric-field intensity underwent a synchronous counterclockwise deflection alongside the current vector. This synergistic rotational behavior of the surface current and internal electric field in the time domain fully substantiates the effective synthesis of orthogonal degenerate modes J_1 and J_2 under a 90° phase difference, thereby verifying that the antenna successfully achieves right-hand CP (RHCP).

3. RESULTS AND DISCUSSION

3.1. S-Parameter and Radiation Efficiency

The S-parameters were measured using an Agilent N6000A vector network analyzer (VNA) calibrated to the hand-soldered SMA connector reference plane via the standard Short-Open-Load-Through (SOLT) technique. The far-field characteristics, including radiation patterns, efficiency, and axial ratio (AR), were characterized in an anechoic chamber (test setup: Figs. 10(a)–(b)). Specifically, the gain and efficiency were measured using the standard gain-transfer method with a calibrated wideband horn antenna, while the AR was determined by measuring the orthogonal linear-polarization components.

Figure 11 compares the measured and simulated S-parameters and radiation efficiency. The results agree well; minor deviations are primarily attributed to practical manufacturing uncertainties, including gap etching tolerances, FR4 dielectric fluctuations, and SMA connector welding errors. Despite these factors, the resonant frequencies remain stable. The measured -10 dB impedance bandwidth is 34.2% (4.38–6.19 GHz) with a center frequency of approximately 5.3 GHz, consistent with the simulated 32.2% (4.41–6.10 GHz). This wide operating bandwidth is effectively distributed around the center frequency to fully cover the targeted 5 GHz WLAN

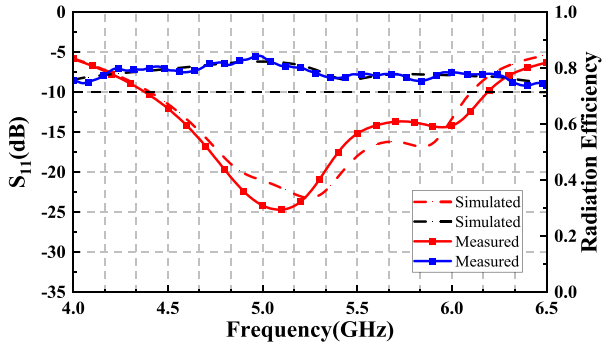

FIGURE 11. Simulated and measured S_{11} and radiation efficiency of the proposed antenna.

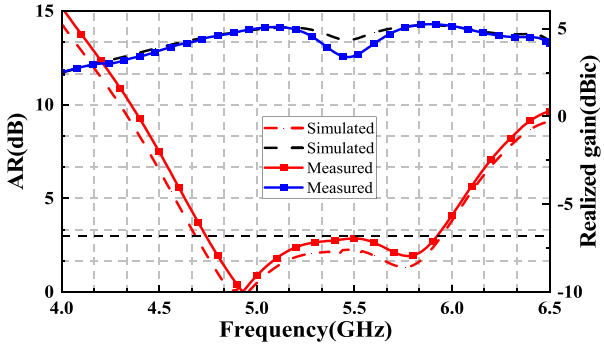

FIGURE 12. Simulated and measured axial ratio and realized gain of the proposed antenna.

TABLE 2. Antenna performance comparison.

Ref.	Frequency (GHz)	Size (λ_0^3)	−10 dB BW (%)	3 dB ARBW (%)	Gain (dBic)
[12]	3.5	$0.58 \times 0.58 \times 0.043$	23.4	8.5	6.57
[14]	5.5	$1 \times 1 \times 0.07$	27.8	20.9	9.7
[17]	5.2	$0.834 \times 0.834 \times 0.04$	37.7	18.3	9
[18]	5.5	$1.4 \times 1.4 \times 0.07$	38.8	14.3	8.5
[19]	3.305	$0.40 \times 0.40 \times 0.044$	29.1	13.47	4.08
[20]	5.5	$0.96 \times 0.96 \times 0.136$	36.3	27.3	9
[21]	5.5	$0.67 \times 0.67 \times 0.065$	39.25	17.7	6.5
This work	5.315	$0.45 \times 0.45 \times 0.047$	34.2	23.9	5.26

λ_0 is the free-space wavelength at center operating frequency

band (5.15–5.85 GHz). Furthermore, the radiation efficiency is maintained above 75% within the operating band. Although inherent material losses and antenna miniaturization typically degrade efficiency, the optimized stepped cross-slot effectively mitigates surface-wave losses and ensures stable radiation performance.

3.2. Axial Ratio and Realized Gain

As depicted in Fig. 12, regarding CP and gain performance, the measured 3 dB AR bandwidth of the proposed antenna is 4.68–5.95 GHz (23.9%), which agrees well with the simulated range of 4.73–5.91 GHz (22.2%). Within this 3 dB AR bandwidth, the measured peak realized gain reaches 5.26 dBic, closely matching the simulated peak realized gain of 5.23 dBic. This gain level reflects an inherent physical tradeoff with antenna miniaturization, primarily constrained by four factors: the reduced radiating aperture size, the inherent dielectric losses of the FR4 substrate, energy dissipation within the feed network, and increased ohmic losses caused by the meandered current paths in the embedded geometry. Despite these physical limitations, the proposed design maintains a good balance among wideband CP, stable gain, and radiation efficiency within a miniaturized footprint.

3.3. Radiation Pattern

Figure 13 shows the numerically simulated and experimentally measured radiation patterns in the *xoz*- and *yoz*-planes at 4.92, 5.315, and 5.77 GHz. The proposed antenna produces a stable and symmetric broadside radiation pattern through right-hand CP (RHCP) radiation. The measured radiation patterns were in good agreement with the simulated results. Furthermore, at all three frequency points, the co-polarization (RHCP) radiation is significantly larger than the cross-polarization (LHCP) radiation in the main beam direction ($+z$-direction), with a minimum difference of more than 15 dB, which indicates high CP purity.

3.4. Performance Comparison

Table 2 provides a detailed comparison of the proposed antenna with recently reported CP antennas, covering key parameters such as dimensions, −10 dB impedance bandwidth (IBW), 3 dB ARBW, and peak gain. The results indicate that the proposed antenna achieves a reasonable balance between miniaturization and operating bandwidth. Its overall dimensions are $0.45 \times 0.45 \times 0.047\lambda_0^3$, which explicitly account for the complete substrate area. Although this footprint is slightly larger than the design in [19], it delivers a considerably wider −10 dB IBW (34.2%) and 3 dB ARBW (23.9%). Specifically, while the design in [20] employs hexagonal parasitic patches to achieve a broader ARBW, it inherently requires significantly larger physical dimensions. Similarly, although the work in [21] utilizes an MTS slot configuration for linear-to-circular polarization conversion, its 3-dB ARBW and miniaturization effect remain limited compared to the proposed antenna. Fur-

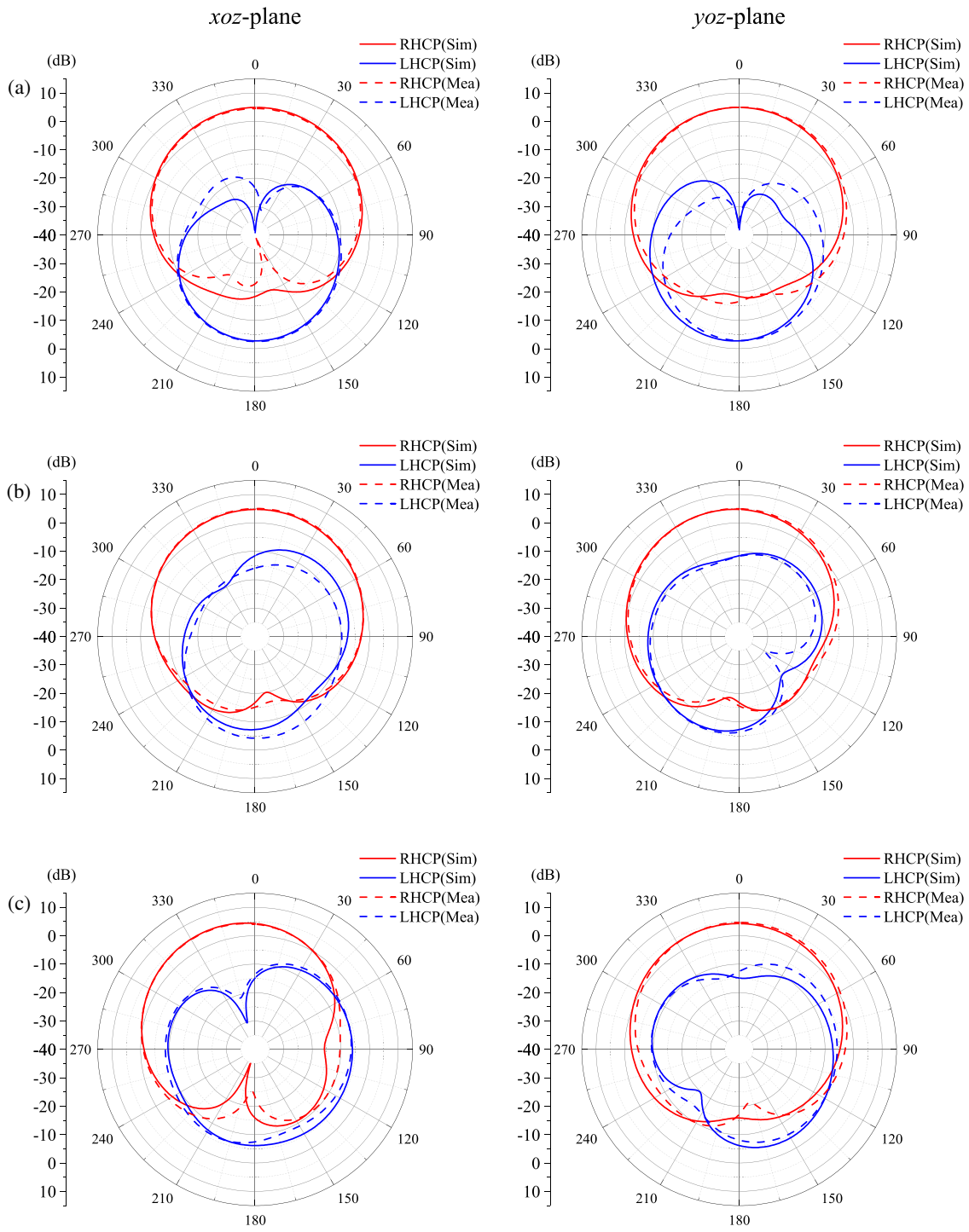

FIGURE 13. Numerically simulated and experimentally measured radiation patterns of the developed antenna at (a) 4.92 GHz, (b) 5.315 GHz, and (c) 5.77 GHz.

thermore, while existing works, such as [14] and [17], exhibit higher peak gains, they rely on larger footprints. Conversely, compared to the designs in [12] and [18], the proposed antenna provides a more distinct miniaturization effect without sacrificing the CP operating band. Although the peak gain is limited to 5.26 dBic due to the reduced radiating aperture, it remains stable and sufficient for practical applications. Consequently, this balanced, miniaturized design provides a useful reference for modern WLAN and 5 GHz wireless communication terminals.

4. CONCLUSION

This study proposes a hybrid embedded CP MTS antenna for WLAN and 5 GHz wireless communication systems. By nesting regular octagonal patches in the primary radiating elements, additional edge capacitance is introduced to shift the resonant frequency downward, effectively achieving antenna miniaturization. Guided by CMA, a sequential slot-coupled feed network is implemented to synchronously excite the orthogonal

degenerate modes with a 90° phase delay. Experimental results validate the design, exhibiting a −10 dB impedance bandwidth of 34.2% (4.38–6.19 GHz) and a 3-dB AR bandwidth of 23.9% (4.68–5.95 GHz). With a stable radiation efficiency over 75% and a peak realized gain of 5.26 dBic, this highly integrated topology provides a valuable reference for the design of modern miniaturized wireless terminals.

ACKNOWLEDGEMENT

This work was supported in part by the Natural Science Research Project of Anhui Educational Committee under Grant No. 2025AHGXZK31006, in part by the Research Foundation of Jiangsu Engineering Research Center for Bionics Control Technology and Equipment under Grant No. FSKZ202503, in part by the Anhui International Joint Research Center for Ancient Architecture Intellisencing and Multi-Dimensional Modeling under Grant No. GJZZX2025KF03.

REFERENCES

[1] Lee, C. S., Y. Fan, and M. Ezzat, "Single-feed circularly polarized microstrip antenna with Bethe holes on the radiating patch," *IEEE Transactions on Antennas and Propagation*, Vol. 68, No. 6, 4935–4938, Jun. 2020.

[2] Ullah, U., M. Al-Hasan, S. Koziel, and I. B. Mabrouk, "A series inclined slot-fed circularly polarized antenna for 5G 28 GHz applications," *IEEE Antennas and Wireless Propagation Letters*, Vol. 20, No. 3, 351–355, Mar. 2021.

[3] Bahrami, S., G. Moloudian, H.-J. Song, and J. L. Buckley, "Reconfigurable UWB circularly polarized slot antenna with three modes of operation and continuous tuning rang," *IEEE Transactions on Antennas and Propagation*, Vol. 70, No. 9, 8542–8547, Sep. 2022.

[4] Ullah, S., Y. He, and Y. Huang, "A triband circular-polarized four-port MIMO antenna with compact size and low mutual coupling," *IEEE Antennas and Wireless Propagation Letters*, Vol. 24, No. 3, 621–625, Mar. 2025.

[5] Sharma, A., G. Das, S. Gupta, and R. K. Gangwar, "Quad-band quad-sense circularly polarized dielectric resonator antenna for GPS/CNSS/WLAN/WiMAX applications," *IEEE Antennas and Wireless Propagation Letters*, Vol. 19, No. 3, 403–407, Mar. 2020.

[6] Li, P., Y. Zhang, X. Qin, K. Wei, P. Liang, and Y. Li, "Wideband widebeam circular-polarized antenna using asymmetrical tri-dipoles for direct satellite-to-handset communications," *IEEE Transactions on Antennas and Propagation*, Vol. 72, No. 8, 6270–6277, Aug. 2024.

[7] Lin, F. H. and Z. N. Chen, "Low-profile wideband metasurface antennas using characteristic mode analysis," *IEEE Transactions on Antennas and Propagation*, Vol. 65, No. 4, 1706–1713, Apr. 2017.

[8] Liu, W. E. I., Z. N. Chen, and X. Qing, "Miniature wideband non-uniform metasurface antenna using equivalent circuit model," *IEEE Transactions on Antennas and Propagation*, Vol. 68, No. 7, 5652–5657, Jul. 2020.

[9] Li, Y. and S. Xiao, "Wideband wide-angle scanning phased array based on miniaturized metasurface antenna," *IEEE Transactions on Antennas and Propagation*, Vol. 70, No. 2, 1107–1119, Feb. 2022.

[10] Li, J., S.-J. Hao, Y.-G. Cui, and X. Chen, "A miniaturized wideband dual-polarized planar antenna based on multiresonance," *IEEE Antennas and Wireless Propagation Letters*, Vol. 21, No. 2, 242–246, Feb. 2022.

[11] Zhang, S., X.-S. Yang, B.-J. Chen, and B.-Z. Wang, "Miniaturized wideband $\pm 45^{\circ}$ dual-polarized metasurface antenna by loading quasi-fractal slot," *IEEE Antennas and Wireless Propagation Letters*, Vol. 22, No. 4, 893–897, Apr. 2023.

[12] Juan, Y., W. Yang, and W. Che, "Miniaturized low-profile circularly polarized metasurface antenna using capacitive loading," *IEEE Transactions on Antennas and Propagation*, Vol. 67, No. 5, 3527–3532, May 2019.

[13] Zeng, J., X. Liang, L. He, F. Guan, F. H. Lin, and J. Zi, "Single-fed triple-mode wideband circularly polarized microstrip antennas using characteristic mode analysis," *IEEE Transactions on Antennas and Propagation*, Vol. 70, No. 2, 846–855, Feb. 2022.

[14] Gao, X., G. Tian, Z. Shou, and S. Li, "A low-profile broadband circularly polarized patch antenna based on characteristic mode analysis," *IEEE Antennas and Wireless Propagation Letters*, Vol. 20, No. 2, 214–218, Feb. 2021.

[15] El Yousfi, A., A. Lamkaddem, K. A. Abdalmalak, and D. Segovia-Vargas, "A broadband circularly polarized single-layer metasurface antenna using characteristic-mode analysis," *IEEE Transactions on Antennas and Propagation*, Vol. 71, No. 4, 3114–3122, Apr. 2023.

[16] Sievenpiper, D., L. Zhang, R. F. J. Broas, N. G. Alexopolous, and E. Yablonovitch, "High-impedance electromagnetic surfaces with a forbidden frequency band," *IEEE Transactions on Microwave Theory and Techniques*, Vol. 47, No. 11, 2059–2074, Nov. 1999.

[17] Wang, Z., W. Ji, M. Wang, W. Wan, and X. Jiang, "Single-layer wideband circularly polarized metasurface antenna with stepped stubs based on characteristic mode analysis," *Progress In Electromagnetics Research Letters*, Vol. 128, 35–40, 2025.

[18] Zhao, C. and C.-F. Wang, "Characteristic mode design of wide band circularly polarized patch antenna consisting of H-shaped unit cells," *IEEE Access*, Vol. 6, 25 292–25 299, 2018.

[19] Swetha, R. and A. Lokam, "Novel design and characterization of wide band hook shaped aperture coupled circularly polarized antenna for 5G application," *Progress In Electromagnetics Research C*, Vol. 113, 161–175, 2021.

[20] Jagtap, S., R. Thakare, and R. K. Gupta, "Low profile, high gain and wideband circularly polarized antennas using hexagonal shape parasitic patches," *Progress In Electromagnetics Research C*, Vol. 95, 15–27, 2019.

[21] Dong, J., C. Ding, and J. Mo, "A low-profile wideband linear-to-circular polarization conversion slot antenna using metasurface," *Materials*, Vol. 13, No. 5, 1164, Mar. 2020.